



## Microstructural characteristics of as-forged and $\beta$ -air-cooled Zr–2.5Nb alloy

Lin-jiang CHAI<sup>1</sup>, Ke CHEN<sup>1</sup>, Shu-yan WANG<sup>1</sup>, Ji-ying XIA<sup>1</sup>, Ting-ting WANG<sup>1</sup>, Zhi-nan YANG<sup>2</sup>

1. College of Materials Science and Engineering, Chongqing University of Technology, Chongqing 400054, China;

2. National Engineering Research Center for Equipment and Technology of Cold Strip Rolling,  
Yanshan University, Qinhuangdao 066004, China

Received 14 April 2017; accepted 4 August 2017

**Abstract:** Multiple characterization and analysis techniques including electron backscatter diffraction (EBSD), electron channeling contrast (ECC) imaging, transmission electron microscopy (TEM) and microhardness test were jointly employed to investigate microstructural characteristics such as local composition, morphology, grain boundary characteristics and interphase orientation relationship of a forged Zr–2.5Nb alloy before and after  $\beta$ -air-cooling. Results show that the as-forged specimen is composed of equiaxed and lamellar  $\alpha$  grains and continuous net-like  $\beta$ -Zr films. After the  $\beta$ -air-cooling, the microstructure of the specimen is featured by basket-weave Widmanstätten structure, in which the inter- $\alpha$ -plate second phases are nanoscale  $\beta$ -Zr. Analyses for crystallographic orientations reveal that the Burgers relationship has been strictly followed during the  $\beta \rightarrow \alpha$  cooling. Compared to the as-forged specimen, the hardness of the  $\beta$ -air-cooled specimen is higher, which could be attributed to the decreased structural sizes of both  $\alpha$  and  $\beta$  phases, and the increased fraction of high angle boundaries as well.

**Key words:** Zr alloy; phase transformation; microstructure; crystallographic orientation

### 1 Introduction

Zirconium (Zr) alloys have long been extensively used in core components in the nuclear power plants because of their high resistance to corrosion and irradiation, as well as satisfactory combination strength and ductility [1–5]. At elevated temperatures, most Zr alloys will experience allotropic phase transformation, i.e.,  $\alpha$ -Zr with a hexagonal close packed (HCP) structure is to be transformed into  $\beta$ -Zr with a body centered cubic (BCC) structure. After a cycle of  $\alpha \rightarrow \beta \rightarrow \alpha$  transformation, distinct microstructures different from those in the starting material are often obtained [6]. During typical fabrications,  $\beta$ -cooling is regarded as a critical step that could greatly affect final performance of Zr alloy products. As such, a number of efforts have been stimulated to reveal microstructural features associated with the  $\beta \rightarrow \alpha$  transformation of Zr alloys. Nowadays, cooling rates, alloying/impurity elements are recognized to be key factors determining their  $\beta$ -transformed microstructures [7]. Nevertheless, earlier efforts have essentially been focused on single-phase Zr alloys such

as Zircaloy-2/4 and Zr702, while much less effort is known on that of dual-phase Zr alloys like Zr–2.5Nb, which has important application (as pressure tubes) in heavy water nuclear reactors [8,9].

In regards to characterization methods by which earlier researchers investigated the  $\beta$ -transformed microstructures in Zr alloys, conventional optical microscopy (OM) and transmission electron microscopy (TEM) were frequently used [10,11]. However, OM and TEM have the deficiencies of rather low magnification and limited field of view, respectively. Also, specimen preparation procedures for OM and TEM are completely different, making specific locations of the interest difficult to be jointly studied by them [12]. As an alternative, the present authors [13–15] have recently noticed that electron channeling contrast (ECC) imaging technique based on field emission gun scanning electron microscope (FEGSEM) allowed clearly revealing various  $\beta$ -cooled microstructural features in a wide field of view, filling the gaps between OM and TEM. In addition, the specimen surface prepared for the ECC observation could be directly used for electron backscatter diffraction (EBSD) characterization to quantify their

**Foundation item:** Project (51401040) supported by the National Natural Science Foundation of China; Project (CSTC2017JCYJAX0114) supported by the Fundamental and Cutting-edge Research Plan of Chongqing, China; Project (E2015203250) supported by the Natural Science Foundation of Hebei Province, China; Project (14LGA005) supported by the Young Teachers Program of Yanshan University, China

**Corresponding author:** Lin-jiang CHAI; Tel: +86-23-62563178; E-mail: [chailinjiang@cqut.edu.cn](mailto:chailinjiang@cqut.edu.cn)

DOI: 10.1016/S1003-6326(18)64769-7

crystallographic orientations [15–17]. The combined use of ECC and EBSD thus allows microstructures of particular interest to be feasibly and accurately characterized and analyzed. In the present work, a dual-phase Zr–2.5Nb alloy was subjected to  $\beta$ -air-cooling treatment and microstructural changes induced by the heat treatment were carefully characterized by use of both FEGSEM-based ECC and EBSD techniques. Results documented in this paper are expected to facilitate better understanding on  $\beta$ -cooled microstructures of dual-phase Zr alloys.

## 2 Experimental

The as-received Zr–2.5Nb alloy was an as-forged rod material with the chemical composition of ~2.5% Nb, ~0.1% Fe, ~0.1% O and Zr balanced (mass fraction). Specimens with dimensions of 12 mm, 8 mm and 1 mm were cut from the as-received material, corresponding to their length direction (LD), width direction (WD) and thickness direction (TD), respectively. Prior to the  $\beta$  treatment, the as-cut specimens were encapsulated in quartz tubes under vacuum ( $\leq 1 \times 10^{-3}$  Pa) to avoid oxidation. The encapsulated specimens were put into a box furnace (SX2–8–16) which had been heated to 1000 °C in advance. After 10 min holding, the specimens were taken out from the furnace and cooled in air (estimated cooling rate of ~5 °C/s [18]).

A FEGSEM (Zeiss Sigma HD) equipped with a back scattering electron (BSE) detector and an electron backscatter diffraction (EBSD) analysis system (Oxford Instruments NordlysMax<sup>2</sup>) was mainly employed for microstructural characterization. The BSE detector was used to produce electron channeling contrast (ECC) images, which were known to be sensitive to crystallographic orientation-related defects [19,20]. For EBSD data acquisition and post-processing, AZtec 2.4 and HKL Channel 5 software packages were used, respectively. Before ECC and EBSD examinations, electro-polishing was performed for the specimens to obtain flat and stress-free surfaces (LD–TD). The analyzed surfaces were immersed in a mixed solution of 10% perchloric acid, 20% butyl cellosolve and 70% methanol (volume fraction), and polished at 20 V and –30 °C for 30–60 s. An FEI Tecnai G2 F20 transmission electron microscope (TEM) and an energy dispersive spectroscopy (EDS) attached to the TEM were also utilized for supplementary microstructure and composition characterization. The TEM foil specimen was prepared using a twin-jet polishing apparatus with a solution of 10% perchloric acid and 90% ethylalcohol (volume fraction). In addition, specimen hardness was measured using a Vickers indentation tester (HVS–1000)

at a load of 100 g for 10 s.

## 3 Results and discussion

### 3.1 ECC observation

Figures 1(a) and (b) show low- and high-magnification ECC images of the as-forged specimen, respectively. The major phase ( $\alpha$ -Zr) appears to be in either equiaxed or lamellar shape, while the continuous net-like films are recognized as  $\beta$ -Zr (the minor phase). The sizes of  $\alpha$  grains are found to be rather scattered, ranging from submicron to above 10  $\mu\text{m}$  (Fig. 1(a)). Thicknesses of the  $\beta$ -Zr films vary from several tens to a few hundreds of nanometers, with an average value of 72 nm (Fig. 1(b)). For  $\alpha$  grains, different image contrasts suggest varied orientations. It is noticed that the  $\beta$ -Zr films generally appear to be brighter than the  $\alpha$  grains, which should be related to atomic-number ( $Z$ ) contrasts of back scattered electrons. With respect to the  $Z$ -contrast, compared to light elements (low atomic number), stronger BSE signals can be produced by heavy elements (high atomic number), leading to higher brightness. For elements involved in the Zr–2.5Nb alloy,  $Z_{\text{Zr}}$ ,  $Z_{\text{Nb}}$ ,  $Z_{\text{Fe}}$  and  $Z_{\text{O}}$  are 40, 41, 26 and 8, respectively. Clearly, the phase containing more Nb is expected to be brighter in the ECC images. It was demonstrated that the maximum solubility of Nb in  $\beta$ -Zr (~20%, mass fraction) was greatly larger than that in  $\alpha$ -Zr (<0.6%) [21] and more than 10% Nb was needed to prevent its decomposition during cooling of Zr–Nb alloys [22]. Thus, it is the more saturated Nb that allows the  $\beta$ -Zr films to be brighter than  $\alpha$  grains in their ECC images.

Figures 1(c) and (d) show low- and high-magnification ECC images of the  $\beta$ -air-cooled specimen. From Fig. 1(c), one can see that the microstructure mainly consists of differently orientated packets, which have substructures of individual parallel-stacked plates and inter-plate thin films (Fig. 1(d)). Such thin films also appear to be brighter than adjacent plates, similar to the case of the as-forged specimen. Inside each packet, rather uniform contrast can be observed for their plates, suggesting the same crystallographic orientation for them. By the linear intercept method, the average width of the plates is measured to be 0.34  $\mu\text{m}$  while the mean thickness of inter-plate films is 55 nm. According to earlier classification [7], the microstructure presented in the  $\beta$ -air-cooled specimen corresponds to basket-weave Widmanstätten structure. A recent work [12] has revealed that plate widths in a dilute Zr–Sn–Nb alloy subjected to the similar  $\beta$ -air-cooling are about 2  $\mu\text{m}$  on average. Comparatively, substructures in the Zr–2.5Nb alloy are largely refined, probably due to the increased amount of the effective  $\beta$ -stabilizing element Nb [23].

### 3.2 TEM characterization

In order to reach more definite recognition on the inter-plate thin films in the  $\beta$ -air-cooled specimen, TEM–EDS analyses have been made and shown in Fig. 2. Figure 2(a) shows a TEM bright-field image of a small location, from which a dislocation-free matrix can be seen. The inter-plate thin films (second phases) in Fig. 1(d) are also observed, as arrowed in Fig. 2(a). EDS analyses for the second phase reveal co-existence of Zr, Nb and Fe (Fig. 2(b)). The Nb content is found to be 19.36% (mass fraction), much higher than its maximum solubility in  $\alpha$ -Zr. The diffusion of Nb was reported to be rather sluggish in Zr alloys [24] and tends to be enriched in residual  $\beta$ -Zr [25]. Combined with the above ECC

results, the inter-plate thin films in the  $\beta$ -air-cooled specimen can be confirmed to be Nb-stabilized residual  $\beta$ -Zr phases. Meanwhile, the consistency between TEM and ECC results also verifies effectiveness of the FEGSEM-based ECC technique in characterizing dual-phase structures (even at nanoscale) in Zr alloys.

### 3.3 EBSD characterization and analysis

EBSD maps scanned for  $\alpha$ -Zr (the major phase) in both the as-received and the  $\beta$ -air-cooled specimens are presented in Fig. 3. Figures 3(a) and (c) show their band contrast (BC) maps, from which one can know that most regions are successfully indexed with high image quality, except a few non-indexed zones (with black contrasts)

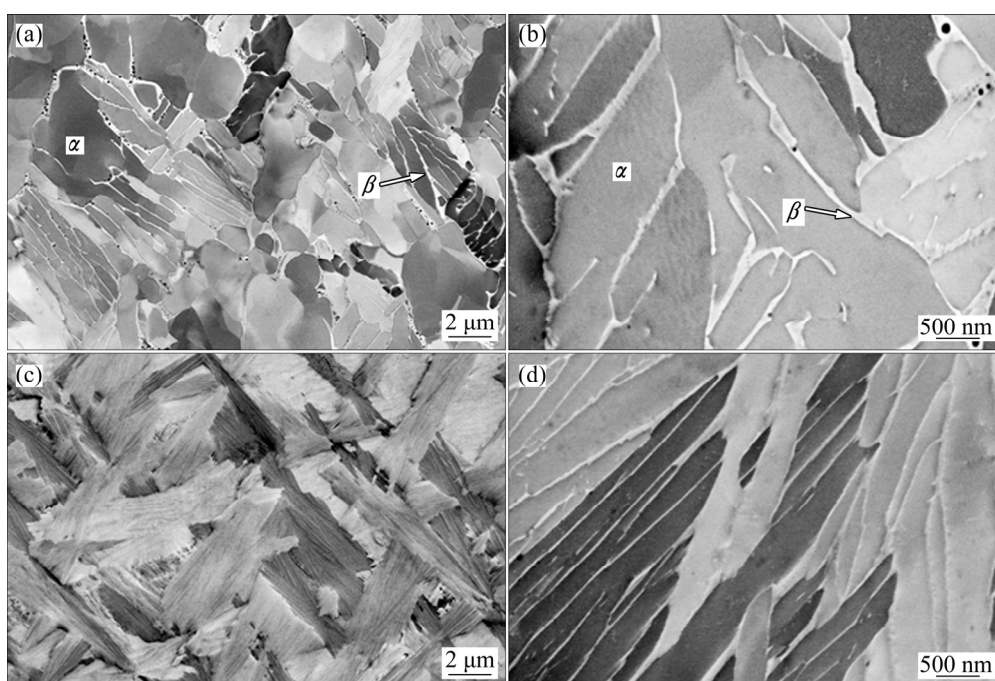


**Fig. 1** Direct ECC observation of Zr–2.5Nb alloy: (a, b) Low- and high-magnification images of as-received specimen, respectively; (c, d) Low- and high-magnification images of  $\beta$ -air-cooled specimen, respectively

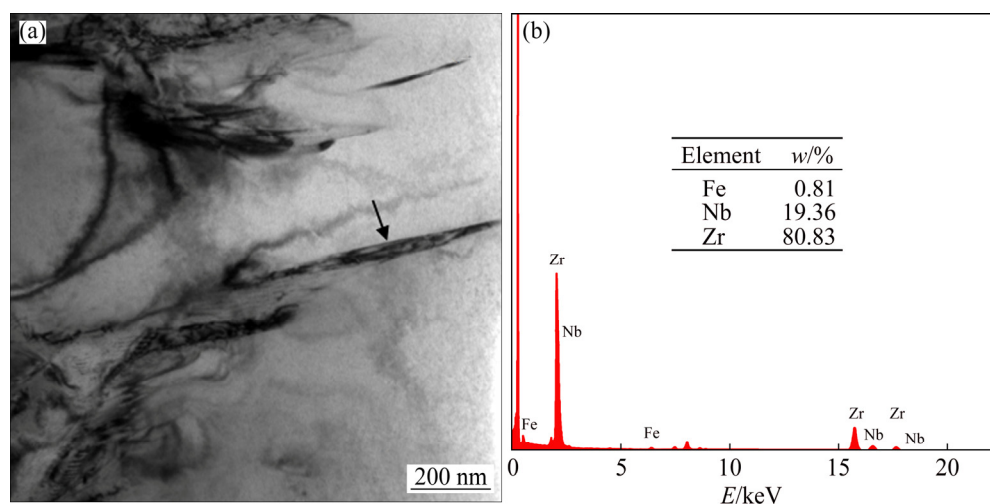


**Fig. 2** TEM bright-field image (a) and EDS result (b) (corresponding to arrowed location) of  $\beta$ -air-cooled Zr–2.5Nb alloy

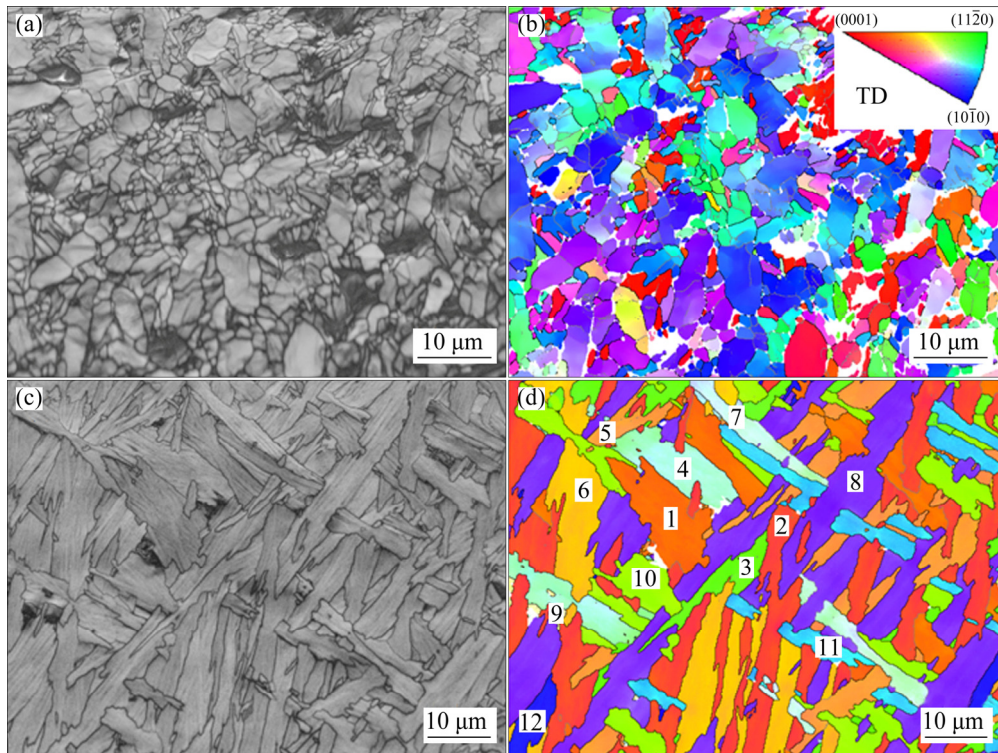


**Fig. 3** EBSD characterization of Zr-2.5Nb alloy: (a, b) BC and OI maps of as-received specimen, respectively; (c, d) BC and OI maps of  $\beta$ -air-cooled specimen, respectively (Black and gray lines in (b) and (d) indicate high and low angle boundaries, respectively; consecutive numbers in (d) indicate various orientations)

due probably to stress concentration. The  $\alpha$ -grain shapes and morphologies revealed by the BC maps are also consistent with direct ECC observation (Fig. 1). Figures 3(b) and (d) show orientation imaging (OI) maps (orientations indicated by colors) of the as-received and the  $\beta$ -air-cooled specimens, respectively. Also, the OI maps are boundaries with  $2^\circ < \theta < 15^\circ$  and  $\theta > 15^\circ$ , i.e., low angle boundaries (LABs) and high angle boundaries (HABs) delineated by black and gray lines, respectively. By means of the grain-reconstruction method [26], the size of each HAB-enclosed grain could be represented by a circle-equivalent diameter after determining its area. This method allows sizes of irregularly-shaped grains to be approximated and compared between specimens. Such calculation gives average sizes of 1.4 and 2.1  $\mu\text{m}$  for  $\alpha$  grains in the as-received and the  $\beta$ -air-cooled specimens, respectively. With respect to specific grains, Fig. 3(d) reveals rather good orientation uniformity for the  $\beta$ -air-cooled specimen. However, grain subdivision seems to exist in the as-forged specimen due to the non-uniform orientations of grains (Fig. 3(b)), similar to the case reported in a rolled commercially pure Zr sheet [27].

Different orientations revealed in Fig. 3(d) appear to be 12, which agrees with the number of  $\alpha$  variants generated by a single  $\beta$  parent according to the Burgers relationship [28]. To further reveal quantitative

relationships between various  $\alpha$  packets in the  $\beta$ -air-cooled specimen, their orientations are projected in  $\{0002\}$  and  $\{11\bar{2}0\}$  pole figures in Fig. 4. From the  $\{0002\}$  pole figure, all the 12 orientations can be grouped into six pairs. For the two orientations in each pair, their  $c$ -axes are found to be coincidentally parallel to each other, for example, orientations 1 and 2. After resorting to the  $\{11\bar{2}0\}$  pole figure, however,  $\langle 11\bar{2}0 \rangle$  directions of the two orientations are noticed to slightly differ from each other by about  $10^\circ$ . This suggests a misorientation of  $\sim 10^\circ / \langle 0001 \rangle$  for every pair of  $\alpha$  orientations, well corresponding to the first Burgers misorientation (Five possible Burgers misorientations exist for any two  $\alpha$  orientations inherited from the same  $\beta$  orientation, i.e.,  $10.5^\circ / \langle 0001 \rangle$ ,  $60^\circ / \langle 11\bar{2}0 \rangle$ ,  $60.8^\circ / \langle 12\bar{3}1 \rangle$ ,  $63.3^\circ / \langle 44\bar{8}3 \rangle$  and  $90^\circ / \langle 12\bar{3}0 \rangle$ ). Again referring to the  $\{11\bar{2}0\}$  pole figure, all the 12 orientations could also be classified as four groups, with each group including three orientations (like those numbered by 1, 5 and 11) sharing one  $\langle 11\bar{2}0 \rangle$  direction. Interestingly, there exists about  $60^\circ$  between basal poles of such grouped orientations, thus being coincident with the second Burgers misorientation ( $60^\circ / \langle 11\bar{2}0 \rangle$ ).

Figures 5(a) and (b) show boundary maps of the as-received and the  $\beta$ -air-cooled specimens, respectively. In addition to common LABs and HABs, boundaries with the Burgers misorientations (denoted as Burgers

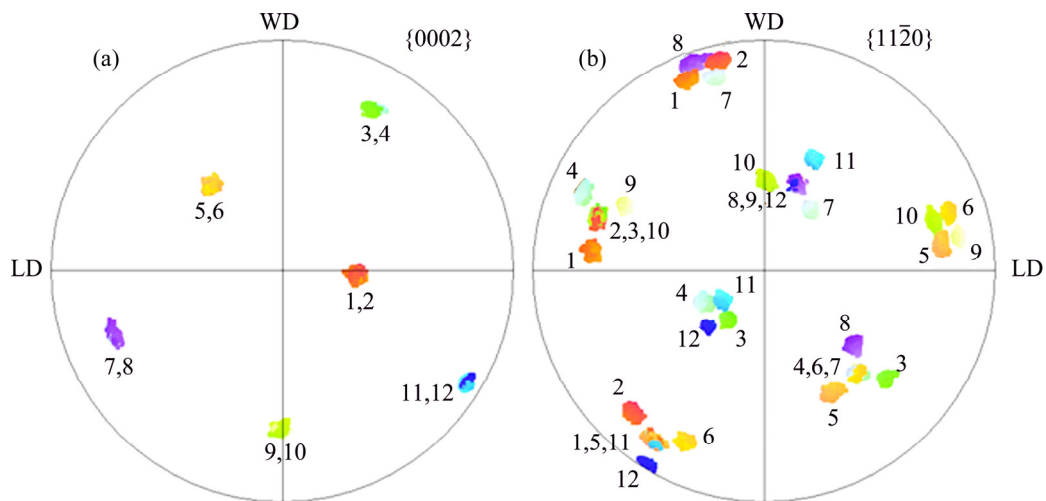


**Fig. 4** {0002} (a) and  $\{11\bar{2}0\}$  (b) pole figures of  $\beta$ -air-cooled Zr-2.5Nb alloy

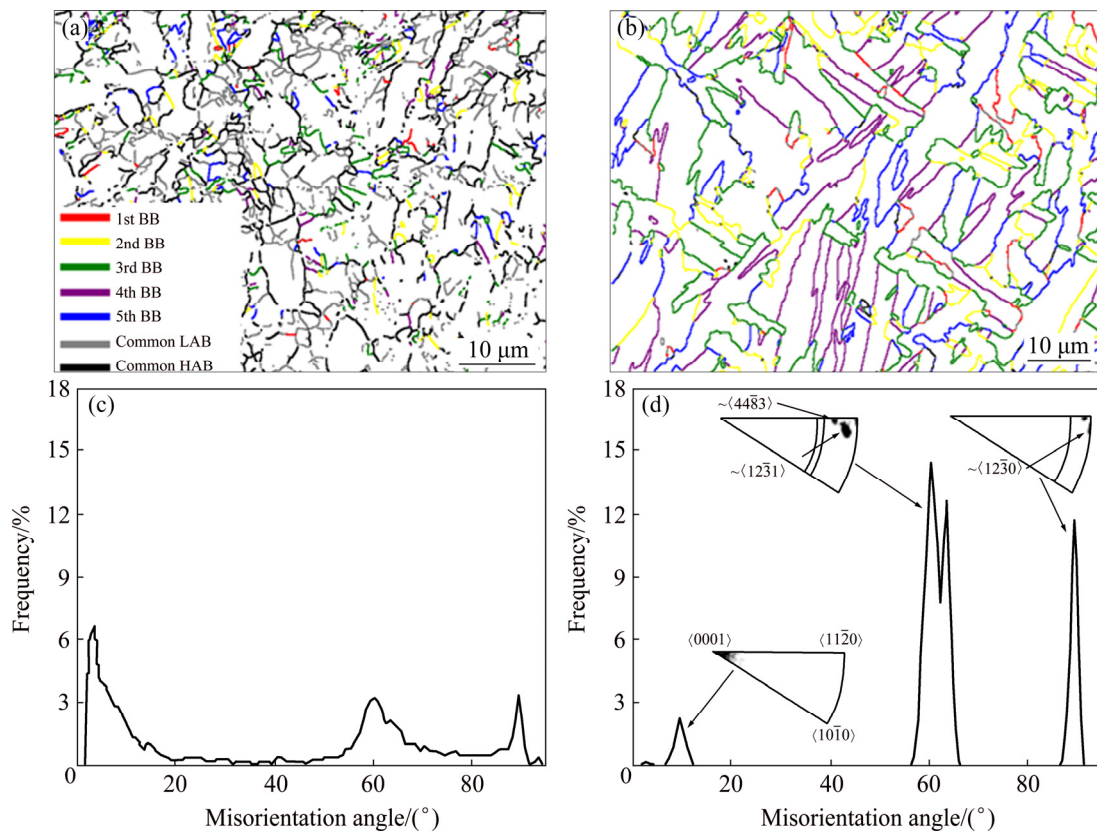


**Fig. 5** Grain boundary maps of as-received (a) and  $\beta$ -air-cooled (b) specimens, and misorientation angle distributions of as-received (c) and  $\beta$ -air-cooled (d) specimens

boundaries (BBs)) are also distinguished by colorful lines. For the as-forged specimen, Fig. 5(a) shows that both the BBs and common boundaries (LABs and HABs) are abundant. Such common boundaries could be related to plastic deformation and/or dynamic recovery/recrystallization during the forging. From Fig. 5(b), however, it can be seen that there are essentially no common boundaries in the  $\beta$ -air-cooled specimen while almost all boundaries belong to the BBs.

Figures 5(c) and (d) present misorientation angle

distribution histograms corresponding to Figs. 5(a) and (b), respectively, allowing fractions of various boundaries to be further quantified. In Fig. 5(c), three evident peaks can be noticed. Among them, the two peaks around 60° and 90° should correspond to the last four Burgers misorientations (Five possible Burgers misorientations exist for any two  $\alpha$  orientations inherited from the same  $\beta$  orientation, i.e., 10.5°/ $\langle 0001 \rangle$ , 60°/ $\langle 11\bar{2}0 \rangle$ , 60.8°/ $\sim \langle 12\bar{3}1 \rangle$ , 63.3°/ $\sim \langle 44\bar{8}3 \rangle$  and 90°/ $\sim \langle 12\bar{3}0 \rangle$ ). Besides, the low angle peak in Fig. 5(c)

confirms the significance of common LABs, especially those with  $\theta < 10^\circ$ . Different from the case in the as-received specimen, no spread of misorientation angles can be seen except three sharp peaks near  $10^\circ$ ,  $60^\circ$  and  $90^\circ$  in the  $\beta$ -air-cooled specimen (Fig. 5(d)). A rotation-axis analysis for its peak near  $60^\circ$  reveals three preferred rotation axes of  $\langle 11\bar{2}0 \rangle$ ,  $\sim \langle 12\bar{3}1 \rangle$  and  $\sim \langle 44\bar{8}3 \rangle$ , suggesting that this peak is superposition of the second, the third and the fourth Burgers misorientations [29]. Similarly, rotation-axis analyses for the peaks near  $10^\circ$  and  $90^\circ$  indicate the first and the fifth Burgers misorientations, respectively. All the above (mis-)orientation-related analyses strongly confirm the strict obedience of the Burgers orientation relationship during the  $\beta \rightarrow \alpha$  cooling of the Zr–2.5Nb alloy.

In earlier work [30] strong  $\alpha$ -variant selection was reported to occur in a Zr–2.5Nb alloy  $\beta$ -treated at a cooling rate of  $\sim 0.3$  °C/s. Such a low rate is believed to give birth to parallel-plate  $\alpha$  structures, which prefer to nucleating at  $\beta$  boundaries along specific habit planes. As a result, only a few favorable  $\alpha$  orientations (variants) could be selected. In the present work, however, the  $\beta$ -air-cooling results in basket-weave  $\alpha$  structures that could nucleate at many sites inside  $\beta$  grains (Figs. 1(c) and 3(c)). Cubic symmetry of the  $\beta$  phase allows more habit planes to be provided [31] so that all the  $\alpha$  variants can be generated, as demonstrated by the above EBSD analyses.

### 3.4 Microhardness test

The average hardness value of the  $\beta$ -air-cooled specimen was measured to be HV 254, larger than that (HV 217) of the as-received specimen. Usually, one may expect reduced grain sizes for specimens with increasing hardness, according to the well-known Hall–Petch effect [32]. However, in the present work, the average size ( $2.1 \mu\text{m}$ ) of  $\alpha$  grains (the major phase) in the  $\beta$ -air-cooled specimen is found to even increase, compared with that ( $1.4 \mu\text{m}$ ) of the as-received specimen. Thickness of  $\beta$ -Zr films is found to decrease from 72 to 55 nm after the  $\beta$ -cooling and their refinement should have contributed to part of the increased hardness. Nevertheless, the  $\beta$ -Zr phase is always the minor constituent, which is not expected to make the major contribution to hardness. Although the measured  $\alpha$ -grain (packet) sizes appear to increase after the  $\beta$ -cooling, it is noticed that fine substructures (submicron  $\alpha$  plates separated by the nanoscale  $\beta$ -Zr films) exist in their interiors (Figs. 1(c), 1(d) and 3(c)). Assuming that dislocations are activated in an  $\alpha$  plate, they cannot easily slip into neighboring  $\alpha$  plates with an identical orientation in the same packet (Fig. 3(d)). This is due to the existence of the inbetween  $\beta$  films, which could actually play a role like HABs in the Hall–Petch model.

It is therefore known that the effective structure ( $\alpha$  plate) impeding dislocation slip is in fact refined, which should be the main reason accounting for the hardness increase in the  $\beta$ -air-cooled specimen. In addition, with respect to boundary types, Fig. 5 shows that the fraction of HABs (including Burgers boundaries with  $\theta > 15^\circ$ ) in the  $\beta$ -air-cooled specimen is evidently higher than that in the as-received specimen. The latter contains more LABs which usually provide smaller impedance than HABs [33] and result in decreased hardness as well.

For phase transformation-induced hardness, its increase in  $\beta$ -cooled Zr alloys has also often been attributed to the solid solution strengthening of alloying elements [12,34]. However, in the present work, the cooling rate offered by the  $\beta$ -air-cooling is relatively low ( $\sim 5^\circ\text{C/s}$ ), which allows sufficient diffusion to occur. As a result, supersaturation of alloying elements in the  $\alpha$ -Zr matrix after rapid quenching could not be expected. During the slow cooling, alloying elements tend to precipitate as second phase particles along  $\alpha$ -plate boundaries in Zircaloy-2/4 [34,35], or are retained in residual  $\beta$ -Zr (element-enriched) along with element-depleted  $\alpha$ -Zr in the Zr–2.5Nb alloy. In fact, we have performed EDS tests (not shown here) for the transformed  $\alpha$  plates and detected hardly any saturated constituents in their interiors, which are consistent with the above analyses. It is therefore known that the solid solution strengthening effect would not make a considerable contribution to the increased hardness of the  $\beta$ -air-cooled specimen.

## 4 Conclusions

1) Detailed microstructural characterization reveals that the as-forged Zr–2.5Nb alloy is composed of  $\alpha$  grains in either equiaxed or lamellar shape and continuous net-like  $\beta$ -Zr films. After the  $\beta$ -air-cooling, the microstructure is featured by basket-weave Widmanstätten structure, in which the second phases inter  $\alpha$  plates are nanoscale  $\beta$ -Zr.

2) The crystallographic orientation examination confirms that the Burgers relationship is strictly obeyed during the  $\beta \rightarrow \alpha$  cooling.

3) Compared with the as-forged specimen, the hardness of the  $\beta$ -air-cooled specimen is higher, which could be attributed to the decreased structural sizes of both  $\alpha$  and  $\beta$  phases, and the increased fraction of high angle boundaries as well.

## References

- [1] MURTY K L, CHARIT I. Texture development and anisotropic deformation of zircalloys [J]. Progress in Nuclear Energy, 2006, 48: 325–359.

- [2] ZHOU B X, YAO M Y, LI Z K, WANG X M, ZHOU J, LONG C S, LIU Q, LUAN B F. Optimization of N18 zirconium alloy for fuel cladding of water reactors [J]. Journal of Materials Science & Technology, 2012, 28: 606–613.
- [3] YAO M Y, SHEN Y F, LI Q, PENG J C, ZHOU B X, ZHANG J L. The effect of final annealing after  $\beta$ -quenching on the corrosion resistance of Zircaloy-4 in lithiated water with 0.04 M LiOH [J]. Journal of Nuclear Materials, 2013, 435: 63–70.
- [4] YUAN G, CAO G, YUE Q, YANG L, YUN Y, SHAO G, HU J. Formation and fine-structures of nano-precipitates in ZIRLO [J]. Journal of Alloys and Compounds, 2016, 687: 451–457.
- [5] YANG Xi-yun, HUANG Hai-qiang, YANG Sheng-hai. Anodic dissolution behavior of zirconium in  $\text{Bu}_4\text{NBr}$ -containing isopropanol solution [J]. Transactions of Nonferrous Metals Society of China, 2016, 26: 2738–2745.
- [6] TEWARI R, SRIVASTAVA D, DEY G K, CHAKRAVARTY J K, BANERJEE S. Microstructural evolution in zirconium based alloys [J]. Journal of Nuclear Materials, 2008, 383: 153–171.
- [7] LUAN Bai-feng, XUE Jiao-jiao, CHAI Lin-jiang, ZHOU Jun. Effect of cooling rates and impurities on the microstructure of  $\beta \rightarrow \alpha$  transformation in Zr alloys [J]. Rare Metal Materials and Engineering, 2013, 42: 2636–2640. (in Chinese)
- [8] KHATAMIAN D. Deuterium diffusion along the three principal directions in anisotropic Zr–2.5Nb [J]. Journal of Alloys and Compounds, 2013, 580: 58–62.
- [9] HIWARKAR V D, SAHOO S K, MANI KRISHNA K V, SAMAJDAR I, DEY G K, SRIVASTAV D, TEWARI R, BANARJEE S, DOHERTY R D. Coarsening of second phase in a two-phase Zr–2.5Nb: On the role of phase boundaries [J]. Acta Materialia, 2009, 57: 5812–5821.
- [10] WOO O T, TANGRI K. Transformation characteristics of rapidly heated and quenched Zircaloy-4-oxygen alloys [J]. Journal of Nuclear Materials, 1979, 79: 83–94.
- [11] KIM H G, BAEK J H, KIM S D, JEONG Y H. Microstructure and corrosion characteristics of Zr–1.5Nb–0.4Sn–0.2Fe–0.1Cr alloy with a beta-annealing [J]. Journal of Nuclear Materials, 2008, 372: 304–311.
- [12] CHAI L, LUAN B, CHEN J, ZHOU J, LIU Q. Effect of cooling rate on  $\beta \rightarrow \alpha$  transformation during quenching of a Zr–0.85Sn–0.4Nb–0.4Fe–0.1Cr–0.05Cu alloy [J]. Science China: Technological Sciences, 2012, 55: 2960–2964.
- [13] CHAI L, CHEN B, WANG S, GUO N, HUANG C, ZHOU Z, HUANG W. Microstructural changes of Zr702 induced by pulsed laser surface treatment [J]. Applied Surface Science, 2016, 364: 61–68.
- [14] CHAI L, CHEN B, WANG S, ZHOU Z, HUANG W. Microstructural characteristics of a commercially pure Zr treated by pulsed laser at different powers [J]. Materials Characterization, 2015, 110: 25–32.
- [15] CHAI L, LUAN B, MURTY K L, LIU Q. Effect of predeformation on microstructural evolution of a Zr alloy during 550–700 °C aging after  $\beta$  quenching [J]. Acta Materialia, 2013, 61: 3099–3109.
- [16] TANG Chao-lan, LI Hao, LI Sai-yi. Effect of processing route on grain refinement in pure copper processed by equal channel angular extrusion [J]. Transactions of Nonferrous Metals Society of China, 2016, 26: 1736–1744.
- [17] HUANG Yuan-chun, YAN Xu-yu, QIU Tao. Microstructure and mechanical properties of cryo-rolled AA6061 Al alloy [J]. Transactions of Nonferrous Metals Society of China, 2016, 26: 12–18.
- [18] CHAI L, LUAN B, CHEN B, YANG H, LIU Q, HUANG W. Concurrent inheritance of microstructure and texture after slow  $\beta \rightarrow \alpha$  cooling of commercially pure Zr [J]. Science China: Technological Sciences, 2016, 59: 1771–1776.
- [19] ZAEFFERER S, ELHAMI N N. Theory and application of electron channelling contrast imaging under controlled diffraction conditions [J]. Acta Materialia, 2014, 75: 20–50.
- [20] ZHOU Zhi-ming, CHAI Lin-jiang, XIAO Zhi-pei, TU Jian, WANG Ya-ping, HUANG Wei-jiu. Surface modification of Cu–25Cr alloy induced by high current pulsed electron beam [J]. Transactions of Nonferrous Metals Society of China, 2015, 25: 1935–1943.
- [21] JEONG Y H, KIM H G, KIM D J, CHOI B K, KIM J H. Influence of Nb concentration in the alpha-matrix on the corrosion behavior of Zr–xNb binary alloys [J]. Journal of Nuclear Materials, 2003, 323: 72–80.
- [22] CHOO K N, KANG Y H, PYUN S I, URBANIC V F. Effect of composition and heat treatment on the microstructure and corrosion behavior of Zr–Nb alloys [J]. Journal of Nuclear Materials, 1994, 209: 226–235.
- [23] SRIVASTAVA D, MUKHOPADHYAY P, BANERJEE S, RANGANATHAN S. Morphology and substructure of lath martensites in dilute Zr–Nb alloys [J]. Materials Science and Engineering A, 2000, 288: 101–110.
- [24] TOFFOLON-MASCLET C, GUILBERT T, BRACHET J C. Study of secondary intermetallic phase precipitation/dissolution in Zr alloys by high temperature–high sensitivity calorimetry [J]. Journal of Nuclear Materials, 2008, 372: 367–378.
- [25] JEONG Y H, LEE K O, KIM H G. Correlation between microstructure and corrosion behavior of Zr–Nb binary alloy [J]. Journal of Nuclear Materials, 2002, 302: 9–19.
- [26] HUMPHREYS F J. Review—Grain and subgrain characterisation by electron backscatter diffraction [J]. Journal of Materials Science, 2001, 36: 3833–3854.
- [27] CHAI L, LUAN B, XIAO D, ZHANG M, MURTY K L, LIU Q. Microstructural and textural evolution of commercially pure Zr sheet rolled at room and liquid nitrogen temperatures [J]. Materials & Design, 2015, 85: 296–308.
- [28] BURGERS W G. On the process of transition of the cubic-body-centered modification into the hexagonal-close-packed modification of zirconium [J]. Physica, 1934, 1: 561–586.
- [29] CHAI L, LUAN B, ZHANG M, MURTY K L, LIU Q. Experimental observation of 12  $\alpha$  variants inherited from one  $\beta$  grain in a Zr alloy [J]. Journal of Nuclear Materials, 2013, 440: 377–381.
- [30] DAYMOND M R, HOLT R A, CAI S, MOSBRUCKER P, VOGEL S C. Texture inheritance and variant selection through an hcp–bcc–hcp phase transformation [J]. Acta Materialia, 2010, 58: 4053–4066.
- [31] HOLT R A. The beta to alpha phase transformation in Zircaloy-4 [J]. Journal of Nuclear Materials, 1970, 35: 322–334.
- [32] YANG H L, KANO S, MATSUKAWA Y, LI Y F, SHEN J J, ZHAO Z S, LI F, SATOH Y, ABE H. Study on recrystallization and correlated mechanical properties in Mo-modified Zr–Nb alloys [J]. Materials Science and Engineering A, 2016, 661: 9–18.
- [33] LUO P, MCDONALD D T, XU W, PALANISAMY S, DARGUSCH M S, XIA K. A modified Hall–Petch relationship in ultrafine-grained titanium recycled from chips by equal channel angular pressing [J]. Scripta Materialia, 2012, 66: 785–788.
- [34] JEONG Y H, RHEEM K S, CHOI C S, KIM Y S. Effect of beta heat treatment on microstructure and nodular corrosion of Zircaloy-4 [J]. Journal of Nuclear Science and Technology, 1993, 30: 154–163.
- [35] MASSIH A R, ANDERSSON T, WITT P, DAHLBÄCK M, LIMBÄCK M. Effect of quenching rate on the  $\beta$ -to- $\alpha$  phase transformation structure in zirconium alloy [J]. Journal of Nuclear Materials, 2003, 322: 138–151.

## 锻态及 $\beta$ 相空冷态 Zr–2.5Nb 合金的显微组织特征

柴林江<sup>1</sup>, 陈可<sup>1</sup>, 王姝伊<sup>1</sup>, 夏吉莺<sup>1</sup>, 王婷婷<sup>1</sup>, 杨志南<sup>2</sup>

1. 重庆理工大学 材料科学与工程学院, 重庆 400054;

2. 燕山大学 国家冷轧板带装备及工艺工程技术研究中心, 秦皇岛 066004

**摘 要:** 应用基于场发射扫描电镜的电子背散射衍射(EBSD)和电子通道衬度(ECC)成像技术, 并结合透射电镜(TEM)及显微硬度测试等表征手段, 对锻态及  $\beta$  相空冷态 Zr–2.5Nb 合金的显微组织(包括微区成分、形貌、晶界特征、相间取向关系等)进行表征。研究发现, 锻态 Zr–2.5Nb 合金的显微组织由等轴或板条状  $\alpha$  晶粒及连续网状  $\beta$ -Zr 薄层构成。经过  $\beta$  相空冷后, 转变成典型的网篮状魏氏组织,  $\alpha$  板条间为纳米级的残余  $\beta$ -Zr。取向分析证实,  $\beta$  相空冷过程  $\beta \rightarrow \alpha$  转变严格遵循 Burgers 取向关系。相对于锻态样品,  $\beta$  相空冷样品的硬度显著增加, 这与其  $\alpha$  板条尺寸及  $\beta$ -Zr 片层厚度的减小以及大角度晶界比例的增加有关。

**关键词:** 锆合金; 相变; 显微组织; 晶体取向

(Edited by Wei-ping CHEN)